Characterization of viscous fingering and channeling for the assessment of polymer-based heavy oil displacements

Sarah Bouquet, Frédéric Douarche, Frédéric Roggero, Sarah Leray

Transport in Porous Media manuscript No.
(will be inserted by the editor)

Characterization of viscous fingering and channeling for the assessment of polymer-based heavy oil displacements

S. Bouquet, F. Douarche, F. Roggero, S. Leray

Received: date / Accepted: date

Abstract The ability to determine a predictive stability criterion is of great practical importance for designing stable polymer-based displacements. Where one usually resorts to a limited number of core-scale experiments or coarse-scale reservoir simulations, the first ones are potentially impacted by lengthscale issues while the second ones possibly smooth out sharp displacing fronts and physical instability due to numerical diffusion. This paper proposes a new hydrodynamical stability criterion based on previous linear stability analysis results. This criterion is tested for 2D polymer oil displacement by performing high viscosity contrasts, high-resolution numerical experiments at pilot scale. We investigate mesh resolution issues and several perturbation ideas. Different factors are considered such as mobility ratios, polymer adsorption and degradation, and heterogeneities. The analysis is based on a combination of reservoir simulation and image processing techniques.

We show the development of viscous fingering in homogeneous porous media is driven by the shock mobility ratio defined as the ratio of the total fluids upstream mobility over the total fluids downstream mobility. This stability criterion proves to predict both the polymer upstream and polymer-free downstream saturation fronts stability, typical of a polymer displacement, whether polymer adsorbs on the rock or degradates, or not. The observed fingers dynamical behavior is in line with previous works addressing single phase miscible flow or immiscible oil displacement in porous media: fingers transversally merge while growing in the flow direction. Time evolution of fingers spreading and number is linear.

Investigation on porous media of variable heterogeneity distributions shows how viscous fingering couples with heterogeneity and leads to even more marked, distorded and unstable flow patterns. In that cases, flow patterns are not solely driven by the porous medium heterogeneity. The more unstable the flow is, the more sensitive it is to heterogeneity. In-depth fingers analysis shows a very specific time evolution behavior, quite different from viscous fingering in homogeneous media. Such a flow pattern is related with production data such

S. Bouquet, F. Douarche, F. Roggero, S. Leray,
IFP Energies nouvelles, Geosciences Division, 1 et 4 avenue de Bois-Préau, 92852 Rueil-Malmaison Cedex, France,
E-mail: sarah.bouquet@ifpen.fr, frederic.douarche@ifpen.fr, frederic.roggero@ifpen.fr
Present address: of S. Leray,
Pontifical Catholic University of Chile, Santiago (UC), Av Libertador Bernardo O'Higgins 340, Santiago, Región Metropolitana, Chili,
E-mail: saleray@ing.puc.cl

as water and polymer breakthrough times and/or oil recovery profiles as a function of time, which can be used in turn to interpret displacement stability and porous medium heterogeneity features.

Keywords Multiphase flow · Porous media · Heavy oil · Viscous fingering · Channeling · Polymer · Mobility ratio · Reservoir simulation · Enhanced oil recovery

1 Introduction

When a viscous fluid filling the voids in a porous medium is driven forward by the pressure of another driving fluid, the interface between them is liable to be unstable if the driving fluid is the less viscous of the two. The existence of viscous fingering due to viscous variations was described long ago by [1,2,3] at small scale. The existence condition for viscous fingering occurs in oil fields and led reservoir engineers to increase the driving fluid viscosity using polymer or foam. While polymer flooding is a proven improved oil recovery method nowadays in the oil and gas industry, the ability to determine a predictive flow stability criterion remains a challenge of great practical importance when considering polymer aqueous solutions as a displacing fluid for heavy oil recovery purposes. This field of application for viscous fluid injection is an opportunity for revisiting the conditions that trigger viscous fingering in porous media.

Porous media involve various and intricated lengthscales that drive fluid flow transport from pore- to large-scale geological units. While such geological bodies constitute tortuous and heterogeneous structures with very contrasted accumulation and transport properties at large scale, they also can be looked at as disordered capillaries networks at small scale. Whereas polymer flooding can macroscopically improve conformance control by smoothing the impact of permeability heterogeneities on fluid flow when considering light to medium oils, the picture is no longer that simple when considering heavy oil displacements. That obviously can lead to viscous instabilities and poor sweep efficiency, which requires careful attention and is a small scale matter first. This lengthscale issue in reservoir simulation is not well accounted for by Darcy-type multiphase flow models aiming at assessing flooding performance. This may lead to erroneous predictions if not simply discarding viscous fingering, because of the coarse space discretization. To that respect, while polymer-based pilots previously performed in Daqing and, more recently, Pelican Lake heavy oil fields proved to be efficient, their modelling and optimal design still constitute a work in progress from a general perspective [4,5,6,7,8].

While one may use a mobility ratio that assumes the flow to be piston-like displacement to predict the flow stability, a more specific mobility ratio would be required for polymer flooding. This has still not been extensively studied in immiscible case with non-linear relative permeability curves (except [9] for the rear front). This paper proposes a new hydrodynamical stability criterion, based on previous linear stability analysis results obtained for immiscible oil displacement in porous media [10,11,12,13]. This criterion is tested for 2D polymer oil displacement by performing high viscosity contrasts, high-resolution numerical experiments at pilot scale. Different factors are considered such as mobility ratios, polymer adsorption and degradation, and heterogeneities. Aside from being two-dimensional (most linear stability analysis results hold for two-dimensional Hele-Shaw-type displacements), the porous medium under consideration is assumed to be water-wet, which facilitates the physical picture of a polymer-based oil displacement since oil is located in large pores.

Moreover, we investigate interaction and competition between heterogeneities and viscous fingering since both may change the sweep efficiency and consequently the recovery.

The channeling due to heterogeneities is generally expected to dominate the flow at large scale [14]. However, the effect of viscous fingering, although at small scale and even when channeling occurs, may not be negligible on oil recovery. The by-passing, i.e. loss in recovery, due to the viscous fingering and due to the channeling was analyzed by [15,16,17,18] for miscible processes. The dominant mechanisms on fluid displacement is is assessed in this paper for immiscible processes and specifically for polymer flooding to make reliable prediction of the recovery process efficiency.

2 Darcy-scale multiphase flow framework and high-resolution model set-up

2.1 Macroscopic equations underlying polymer flooding models in porous media

We consider immiscible two-phase flow in a porous medium in the presence of polymer. We distinguish two phases: an aqueous and an oil phase, denoted w and o. This flow is modified by the presence of dissolved polymer molecules in water. Polymer is transported by the water phase, which requires to solve an additional mass balance equation. Polymer is either mobile or adsorbed on the rock.

Water viscosity can be very significantly increased when polymer is added to water [17], which has led many authors to model polymer by applying a mobility reduction factor to the water mobility when polymer is present [19,17]. Thus, to describe the water and hydrocarbon phases, we consider a black-oil model [20,21] where the water phase involves a modified velocity which will be denoted $\mathbf{u}_w^p$. The mass conservation equations read:

$$\begin{cases} \partial_t(\Phi\rho_w S_w) + \nabla\cdot(\rho_w \mathbf{u}_w) = q_w \\ \partial_t(\Phi\rho_w S_w C_w^p + (1-\Phi)\rho_r C_r^p) + \nabla\cdot(\rho_w \mathbf{u}_w^p C_w^p) = q_w C_w^p \\ \partial_t(\Phi\rho_o S_o) + \nabla\cdot(\rho_o \mathbf{u}_o) = q_o \end{cases} \tag{1}$$

where Φ is the rock porosity. For each phase denoted $\alpha = w,o$, S_α is the saturation, ρ_α the density and q_α the source/sink term per unit volume of porous medium. C_w^p stands for the flowing polymer mass fraction in the water phase and C_r^p for the adsorbed polymer mass fraction on the rock with ρ_r the rock density. Mobile and adsorbed polymer mass fractions are related with an adsorption law such as a Langmuir isotherm [22,23].

Under laminar flow conditions, the averaged macroscopic pure phase velocities in permeable porous media are governed by the generalized Darcy law:

$$\mathbf{u}_\alpha = -\frac{k_{r\alpha}}{\mu_\alpha}\mathbf{k}\cdot(\nabla P_\alpha - \rho_\alpha \mathbf{g}) \tag{2}$$

where $\mathbf{k}$ is the rock permeability tensor, μ_α the pure phase viscosity, P_α the pressure of the phase α and $\mathbf{g}$ the gravity acceleration. $k_{r\alpha}$ is the relative permeability for the pure phase α, i.e. without polymer. We suppose the relative permeabilities and capillary pressure $P_c = P_o - P_w$ functions depend on water saturation only and are known, with given saturation end points.

In order to simplify the notations in the following, we introduce the phase mobility $\lambda_\alpha = k_{r\alpha}/\mu_\alpha$ and the phase fractional flow $f_\alpha = |\mathbf{u}_\alpha|/|\mathbf{u}|$ where the total velocity $\mathbf{u} = \sum_{\alpha=w,o}\mathbf{u}_\alpha$ is the sum of the phase velocities [24]. The water mobility λ_w^p in the presence of polymer is scaled by a mobility reduction function R_m, also referred as to "resistance factor" by some authors. Hence, the polymer solution velocity reads:

$$\mathbf{u}_w^p = -\lambda_w^p \mathbf{k}\cdot(\nabla P_w - \rho_w \mathbf{g}) \quad \text{with} \quad \lambda_w^p = \frac{\lambda_w}{R_m} \tag{3}$$

where λ_w^p is the modified water mobility in the presence of polymer. The mobility reduction R_m is a multi-parameter interpolation function that accounts for water viscosity variations due to aqueous polymer and salts concentrations, permeability reduction due to adsorbed polymer molecules on the rock and polymer solution shear-thinning rheological behavior. Thus, it depends on mobile and adsorbed polymer concentrations C_w^p and C_r^p, water salinity and shear rate.

This work does not consider the permeability reduction induced by adsorbed polymer molecules nor the mobility reduction salinity and shear rate dependency. It does not consider polymer inaccessible pore volume either [19,17]. Thus, the mobility reduction R_m is a function of the mobile polymer concentration C_w^p only. IFP Energies nouvelles reservoir simulator PumaFlow [25] is considered herein for the only purpose of demonstrating the results of this paper. To finish with, the water-oil capillary pressure is neglected in this work. We explain why hereafter in Section 2.2 when setting-up the physical model.

The main purpose of this work is to probe and predict the hydrodynamical stability of heavy oil displacements by polymer solutions for different flow conditions, varying the injected fluid viscosity. Specifically, the porous medium under consideration is two-dimensional and saturated with a 1500 cP viscous oil. Whereas one expects the waterflooding (without polymer) to yield unstable displacement profiles with poor sweep efficiency due to viscous fingering, polymer injection, when properly designed, is thought to deliver a stable displacing profile for some optimal mobility reduction threshold to be determined. This threshold is numerically determined using numerical simulation experiments and translated into a predictive mobility ratio criterion that governs the flow hydrodynamical stability. This mobility ratio criterion is then tested on several fluid flow configurations and validated. Eventually, flow configurations where polymer adsorbs on the rock or degradates are also considered. The ability to determine a predictive stability criterion is of great practical importance for designing stable porous media displacements, where one usually resorts to a limited number of core-scale experiments potentially impacted by lengthscale issues and coarse-scale reservoir simulations that possibly smooth out sharp displacing fronts and physical instability due to numerical diffusion.

2.2 High-resolution numerical model set-up

The porous medium under consideration is a two-dimensional x-y square plate that corresponds to a homogeneous and isotropic water-wet unconsolidated sandstone reservoir which is saturated with a 1500 cP viscous heavy oil. Its average properties, reported in Table 1, have been adapted from Pelican Lake polymer pilot [7]. Two straight parallel x-y horizontal injection and production wells with a length of 175 m are facing each other and are located at the reservoir boundaries at $x = 0$ and $x = L$ for all $0 \leq y \leq L$, respectively. Water and oil relative permeabilities are assumed to be power law functions of the water saturation, that is $k_{rw} = k_{rw}^0(S)^{n_w}$ and $k_{ro} = k_{ro}^0(1-S)^{n_o}$ with $S = \frac{S_w - S_{wi}}{1 - S_{orw} - S_{wi}}$ the normalized mobile water saturation, S_{wi} the water irreducible water saturation and S_{orw} the residual oil saturation. Initial water saturation is set to a slightly larger value than the irreducible water saturation, that is $S_w(\mathbf{x}, t = 0) = S_{wi} + \varepsilon$ with $\varepsilon = 0.03$ for all (x,y) in $[0,L] \times [0,L]$, to mimic the effect of an early depletion of the reservoir. Rock compressibility is assumed to be negligible. A constant water injection flow rate of $q_w = 5.75$ m^3/day is imposed at in-situ conditions.

Because the porous medium under consideration is homogeneous, viscous fingering cannot initiate when simulating the displacement of a 1500 cP viscous oil by water. Viscous fingering, whenever it should initiate and grow, has to be triggered by some perturbation in

Table 1: Two-dimensional porous medium properties.

GEOMETRY	$(\text{Length}, \text{Width}, \text{Thickness}) = (L, L, H) = (175, 175, 2.4)$ m
WELLS	Two parallel horizontal wells facing each other (175 m length/spacing) Constant injection flow rate (in-situ conditions) $q_w(t) = 5.75$ m^3/day Constant production bottom-hole pressure $P_{\text{BH}}(t) = 20$ bar
FLUID PROPERTIES	Oil density $\rho_o(T,P) = 970$ kg/m^3 Oil viscosity $\mu_o(T,P) = 1500$ cP Water density $\rho_w(T,P) = 970$ kg/m^3 Water viscosity $\mu_w(T,P) = 1$ cP
PETROPHYSICS	Average homogeneous porosity $\Phi = 0.35$ Average homogeneous isotropic permeability $k = 4$ D
RELATIVE PERMEABILITIES	Saturations end points $S_{wi} = 0.22$ and $S_{orw} = 0.2$ Corresponding relative permeabilities $k^0_{ro} = 1$ and $k^0_{rw} = 0.2$ Relative permeabilities exponents $n_w = 4$ and $n_o = 2$
INITIAL CONDITIONS	Initial pressure $P(\mathbf{x}, t = 0) = 21$ bar Constant temperature $T(\mathbf{x}, t) = 16\ ^\circ$C Initial water saturation $S_w(\mathbf{x}, t = 0) = S_{wi} + \varepsilon = 0.25, \varepsilon = 0.03$

the same way Saffman and Taylor proceeded in their 1958 paper [1,26]. If the displacement is stable, the water saturation front will remain stable and the flow computation will converge to the perturbation-free case, and if the displacement is unstable, fingers will initiate and grow. This perturbation can be set as a permeability/porosity noise [17,27] or a locally perturbed saturation initial state [28,29,30]. Doing so, one has to make sure the flow pattern to be obtained does not depend on the perturbation, which may in turn depend on the porous medium spatial discretization [2]. Therefore, a sensitivity study has been first conducted on the perturbation scheme and the mesh resolution in order to define the more appropriate bias-free perturbation scheme and spatial discretization while ensuring the flow computation numerical convergence.

Flow simulations are conducted on a cartesian grid using a nine-point scheme in order to reduce grid-orientation effects. Three x-y discretizations are considered: $\Delta x = \Delta y = 1$, 0.5 and 0.25 m. Two types of perturbation are evaluated. The first one is a permeability and porosity noise, $\delta k(\mathbf{x})$ and $\delta\Phi(\mathbf{x})$, which is superimposed to the reservoir constant permeability and porosity. Porosity and permeability fields are Gaussian and log-normal distributed, spatially uncorrelated, with average values m_k and m_Φ that correspond to the reservoir constant permeability k and porosity Φ, and with small standard deviations σ_k and σ_Φ that account for perturbations (see Table 2).

Table 2: Log-normal permeability and Gaussian porosity fields for different standard deviations σ, keeping the mean m constant (no spatial correlation).

Φ/k distributions	m_Φ (-)	σ_Φ (-)	m_k (mD)	σ_k (mD)
Model 1	0.35	0.0175	4000	400 (10% of m_k)
Model 2	0.35	0.0175	4000	200 (5% of m_k)
Model 3	0.35	0.0035	4000	40 (1% of m_k)

The other perturbation scheme locally adds noise to the initial water saturation in the vicinity of the injection well while keeping constant the reservoir permeability and porosity. Specifically, we set $S_w = S^0_w + \delta S_w$ for $0 \leq x \leq n\Delta x$, $0 \leq y \leq L$ and $t = 0$ where $S^0_w = S_{wi} + \varepsilon$

denotes the unperturbed initial water saturation and δS_w a centered Gaussian noise that only acts over the $0 \leq x \leq n\Delta x$ slice with $n = 2$. Three configurations that correspond to a relative saturation perturbation $\sigma_{\delta S_w}/S_w^0$ of 4%, 8% and 16% are considered hereafter. This spatially-bounded perturbation leads to an initial "saturation fringe" close the injection well, and does not extend over the whole domain as for the previous permeability and porosity perturbation scheme.

The relevance of these two perturbation schemes and the robustness of the resulting in-situ profiles are discussed in the next Section.

2.3 Fingers analysis methodology

In order to analyze the fingers in-situ initiation and growth as a function of space and time (or injected pore volume [1]), we propose the following methodology:

- The fluids two-dimensional dynamical distributions are analyzed through binary images which discriminate the displacing front (with or without fingers) that separates upstream-displacing and downstream-displaced saturation fields. In the case of an unstable displacement, that is for some unfavorable mobility ratio criterion (to be defined and validated hereafter), fingers develop at this front and grow.
- Fingers maximum and minimum lengths are calculated from these binary images in order to dynamically monitor the displacement front in terms of the most advanced fingertip.
- Then, the fingers spreading, which is defined as the difference between the maximum and minimum fingers advances, and the median location of the fingers are calculated, as highlighted in Fig. 1a.
- Eventually, the number of fingers is counted at the front median location, as depicted in Fig. 1b.

In Sections 3 and 4, these quantities are normalized when indicated by the subscript *. The number of fingers is normalized by the maximum number of fingers, finger tip location and fingers spreading are normalized by the domain size. Time will also be normalized by water or polymer breakthrough time.

2.4 Building a weakly perturbed model

We now simulate water injection using three space discretizations $\Delta x = \Delta y$ of 1, 0.5 and 0.25 m and the porosity/permeability perturbation scheme referred as to "model 1" in Section 2.2. Perturbation is applied to the coarsest grid then downscaled to the finest grids by replicating k-Φ values. Noise-free k-Φ reference cases have been simulated as well in order to check that the simulator does not introduce any numerical errors while computing converged stable solutions, and to highlight the need for a perturbation to render viscous fingering.

Fig. 2 reports the obtained saturation profiles when 0.08 pore volume of water has been injected into the reservoir, and clearly demonstrates that the perturbation-free case does not develop any finger but a sharp and stable saturation front $S_f = 0.37$ (see also Fig. 9a) whereas fingers develop when applying a k-Φ perturbation. Fingers look sharper and more numerous when improving the space discretization and their mean positions are very close.

[1] Injected pore volume is a convenient time scale which is defined as the ratio of the cumulative injected fluid volume over the medium pore volume

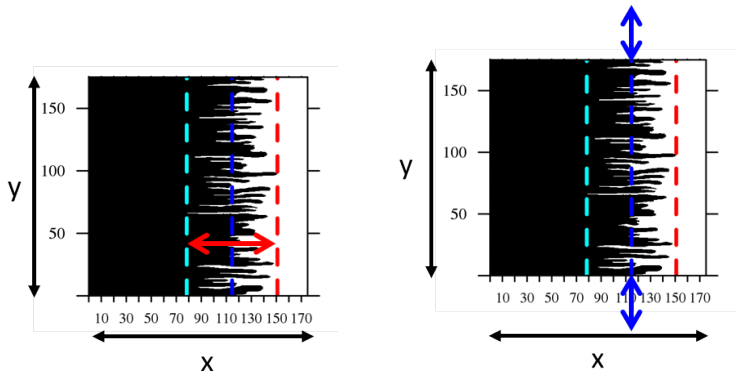

(a) Fingers spreading (red arrow) is computed from the fingers maximum and minimum advances (dashed red and cyan lines).

(b) Fingers number is counted at the median location (dashed blue line).

Fig. 1: Binary image of the in-situ displacing fluid saturation profile highlighting the displacement front and fingers distribution. X and Y coordinates are in meters.

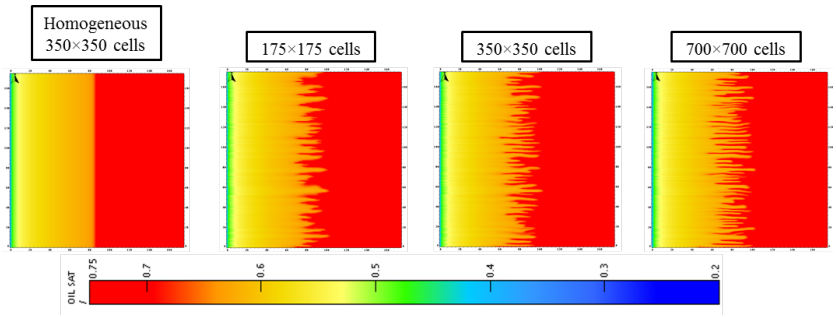

Fig. 2: Comparison of saturation profiles after 0.08 pore volume of water injection when considering homogeneous and porosity/permeability-perturbed models, and three spatial discretizations.

Fig. 3 reports fingers dynamical behavior features such as fingers number and spreading, as a function of the injected pore volume before water breakthrough. It shows that fingers merge (number of fingers decreases with time) whereas fingers spreading increases with time. Fingers merge and spreading both evolve linearly with time or injected pore volume. The 350×350- and 700×700-cells grids deliver approximately the same results whereas the coarsest 175×175-cells grid exhibits some noticable differences. This convergence trend led us to consider the 350×350 grid with $\Delta x = 0.5$ m.

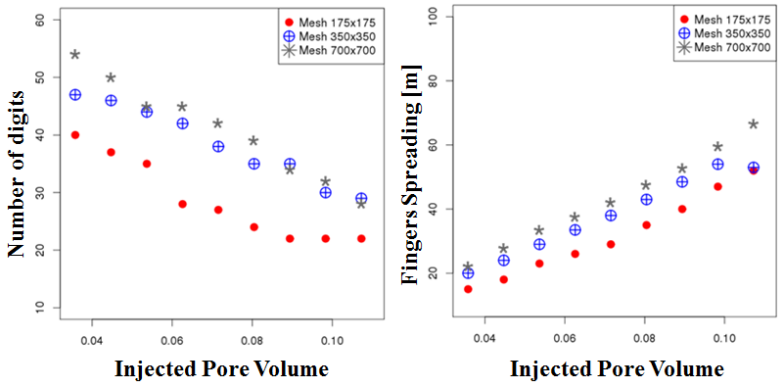

Fig. 3: Fingers dynamical behavior using a k-Φ perturbation for different space discretizations. The number of fingers decreases as a function of the injected pore volume (left figure) while the fingers spreading increases as a function of the injected pore volume (right figure).

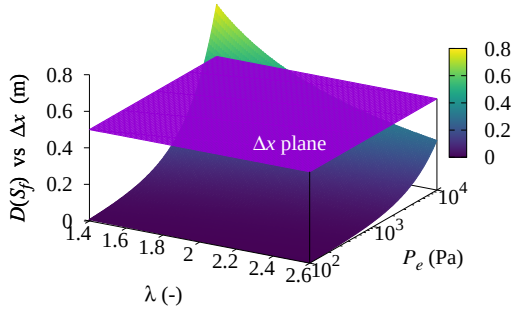

Fig. 4: Comparison of the P_c-driven front spreading length $\mathscr{D}(S_f)$ estimate given by Eq. (4) with the spatial discretization $\Delta x = \Delta y = 0.5$ m as a function of entry pressure and pore size distribution index (see the text).

The water-oil capillary pressure has been neglected so far. For a one-dimensional incompressible displacement of oil by water, transport equation reads, neglecting gravity [24]:

$$\frac{\partial S_w}{\partial t} + \frac{u}{\Phi}\frac{\partial f_w}{\partial x} = 0 \quad \text{with} \quad f_w = \mathscr{F} + \mathscr{D}\frac{\partial S_w}{\partial x} \quad \text{and} \quad \begin{cases} \mathscr{F} = \dfrac{1}{1+\frac{\lambda_o}{\lambda_w}} \\ \mathscr{D} = \dfrac{k}{u}\dfrac{\lambda_o}{1+\frac{\lambda_o}{\lambda_w}}\dfrac{\mathrm{d}P_c}{\mathrm{d}S_w} \end{cases} \tag{4}$$

Using the chain rule, one gets:

$$\frac{\partial S_w}{\partial t} + \frac{u}{\Phi}\left[\frac{\mathrm{d}\mathscr{F}}{\mathrm{d}S_w}\frac{\partial S_w}{\partial x} + \frac{\partial}{\partial x}\left(\mathscr{D}\frac{\partial S_w}{\partial x}\right)\right] = 0 \tag{5}$$

It can be shown that the diffusion-like capillary-pressure-driven function $\mathscr{D}$, which is homogeneous to a length, spreads the Buckley-Leverett displacing water saturation front [10,

24]. As a consequence, when meshing the porous medium saturated with heavy oil to be flooded by water, the gridblock size has to be set smaller than $\mathscr{D}$ in order to render capillary pressure effects. Let us estimate this $\mathscr{D}(S_f)$ function given by Eq. (4), and compare that lengthscale with the space discretization Δx of the numerical model. Writing the capillary pressure $P_c = P_e/S^{1/\lambda}$ where $P_e \geq 0$ denotes the porous medium entry capillary pressure, λ the pore size distribution index and S the normalized mobile water saturation [31], we can estimate this P_c-driven spreading length, knowing that P_e is about or lower than 0.1 bar for a highly permeable unconsolidated sandstone [32].

Fig. 4 shows that this front capillary spreading length is way lower than the spatial discretization of 0.5 m when considering various entry pressures and pore size distribution indexes. As a consequence, capillary pressure effect is expected to be very small in the x-flow direction for the considered rock-fluid system. In particular, its effect in term of front diffusion should be smaller than the numerical diffusion in this work. Transverse effect (in the y-coordinate) of capillary pressure on fingers dynamics may slightly impact fingers merging but is not considered in this work.

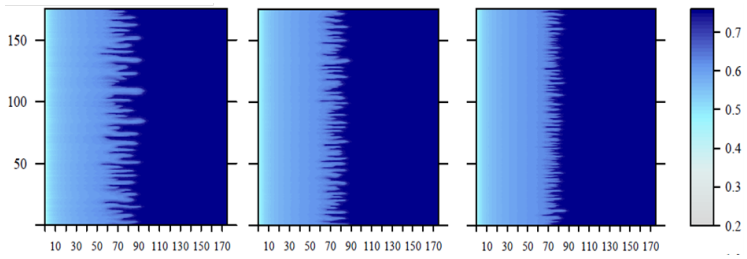

Fig. 5: Comparison of saturation profiles after 0.08 pore volume of water injection for different permeability standard deviations of 10%, 5% and 1% of the average permeability (left to right; see Table 2).

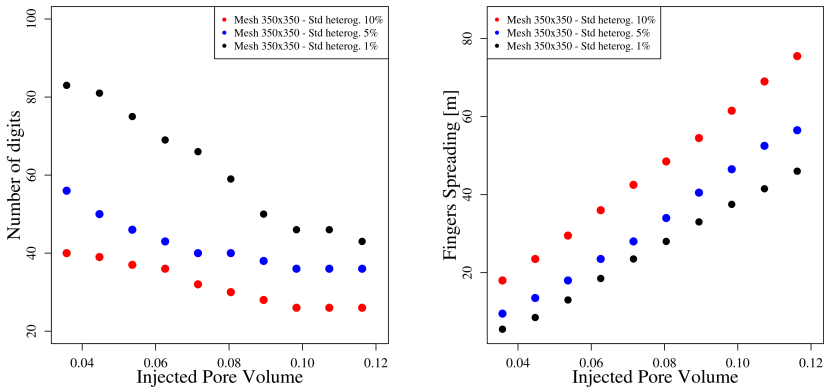

Fig. 6: Fingers dynamical behavior using different permeability noises whose standard deviation is 10%, 5% and 1% of the average permeability (see Table 2): fingers number decreases with time (left figure) while fingers spreading increases with time (right figure).

We now probe how the fingers number and spreading dynamical behavior depends on the perturbation scheme. So far we considered a k-Φ noise over the entire domain (denoted "model 1"), varying the spatial discretization. The three k-Φ perturbation models reported in Table 2 are now considered. Fig. 5 shows that increasing the permeability noise variance accelerates the fingers growth and spreading; specifically, Fig. 6 shows that the number of fingers for the lowest permeability variance is about twice the number of fingers for the highest variance. The inverse trend is observed for the fingers spreading: the higher the variance, the higher the fingers spreading. Because of that significant effect of permeability noise on fingers time evolution, this perturbation has not be retained in this work.

The other "saturation fringe" perturbation method yields more consistent results: the fingers behavior is similar for all the considered standard deviations, as reported in Fig. 7. Specifically, the fingers number and spreading are very close when varying the saturation perturbation, as shown in Fig. 8. Therefore, this perturbation scheme has been retained to trigger the flow instability when the specific conditions are met, as explained in the next Section.

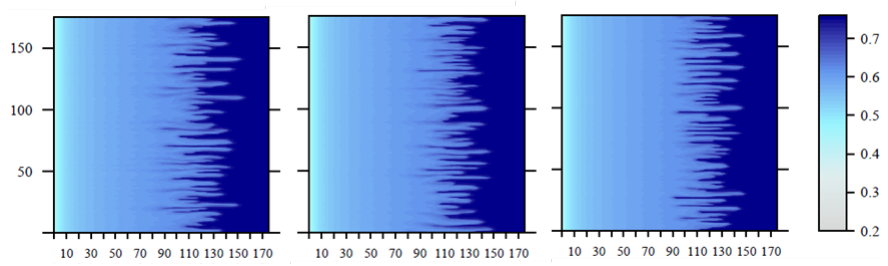

Fig. 7: Comparison of saturation profiles after 0.12 pore volume of water injection for different inlet saturation standard deviation of 16%, 8% and 4% of the noise-free initial saturation (from left to right).

2.5 Stability criteria zoo

The main objective of this work is to define and validate by numerical experiments a stability criterion which predicts the stability of polymer-based displacements in porous media. While many authors, especially Hagoort, Yortsos, Artus and co-workers [10, 11, 13], have established stability criteria using linear stability analysis for waterflooding (immiscible water-oil displacement), the question remains not fully answered when validating the relevance of these criteria by numerical simulation or displacement experiments. The question remains open for two-dimensional polymer flooding and three dimensional displacements in porous media.

Fig. 9a illustrates the water saturation front S_f which forms for waterflooding and separates the upstream displacing fluid(s) from the downstream displaced fluid(s). Such a displacement is said to be unstable if some mobility ratio, to be defined, is larger than one, that is when the upstream fluid(s) mobility is larger than the downstream one, and vice versa. It is worth nothing that, when lacking reliable fluid flow characterization, many oil and gas professionals use the "rule-of-thumb" mobility ratio M_0 which is defined as the ratio of the

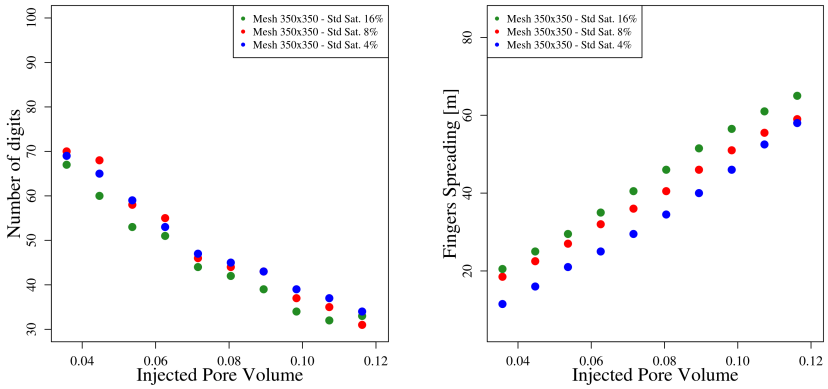

Fig. 8: Fingers dynamical behavior using different inlet saturation noise standard deviation: fingers number decreases with time (left figure) while fingers spreading increases with time (right figure).

maximum water mobility over the maximum oil mobility [33,12,34]:

$$M_0 = \frac{\lambda_w^0}{\lambda_o^0} = \frac{\mu_o}{\mu_w}\frac{k_{rw}^0}{k_{ro}^0} \tag{6}$$

where k_{rw}^0 and k_{ro}^0 denote the maximum water and oil relative permeabilities. This stability criterion assumes the displacement to be piston-like and discards any saturation dependency by assuming the displacing fluid profile to be shaped like a Heaviside step function. In fact, nothing could be farther from the truth, as reminded by Fig. 9a.

Following partly Hagoort, Yortsos, Artus and co-workers [10,11,13], we propose two families of stability criteria, or "shock mobility ratios", which read:

$$M = \begin{cases} \dfrac{\lambda_w^-}{(\lambda_w+\lambda_o)^+} & (M_a) \\ \dfrac{(\lambda_w+\lambda_o)^-}{(\lambda_w+\lambda_o)^+} & (M_b) \end{cases} \quad \text{and} \quad M = \begin{cases} \dfrac{\langle\lambda_w+\lambda_o\rangle^-}{(\lambda_w+\lambda_o)^+} & (M_c) \\ \dfrac{(\frac{1}{\lambda_w+\lambda_o})^+}{\langle\frac{1}{\lambda_w+\lambda_o}\rangle^-} & (M_d) \end{cases} \tag{7}$$

Specifically :

- M_a and M_b compare locally the fluids mobilities $\lambda_\alpha^\pm = k_{r\alpha}(S_f^\pm)/\mu_\alpha^\pm$ upstream and downstream the front vicinity, which is denoted $S_f^\pm$ (see Fig. 9a). Superscripts $^-$ and $^+$ refer to upstream and dowstream the front vicinity. M_a differs from M_b by considering water as the upstream displacing fluid whereas M_b sums water and oil mobilities upstream the front. M_b is the shock mobility ratio derived from linear stability analysis for waterflooding by [10,12,11,13].
- M_c and M_d define an average mobility upstream the front by integrating the full saturation tail through $\langle f\rangle = \frac{1}{x_f}\int_0^{x_f} f(x)\,\mathrm{d}x$. M_c averages the total mobility upstream the front whereas M_d averages the reciprocal total mobility upstream the front [24,34].

To sum up, M_a and M_b are local and shock-related mobility ratios whereas M_c and M_d account for the saturation history upstream the front.

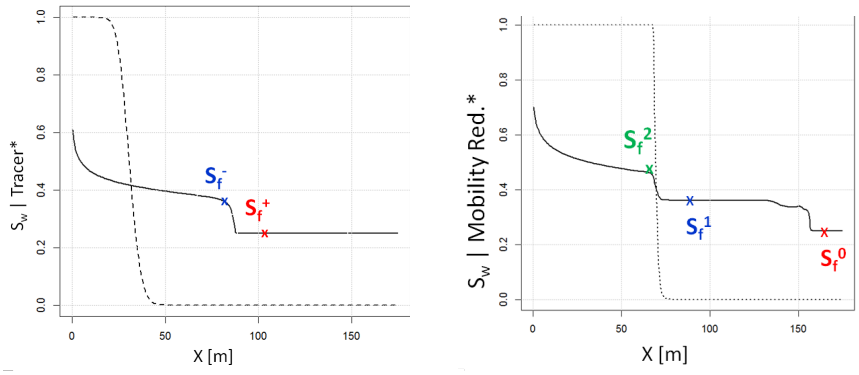

(a) Waterflooding. This saturation profile shows the rarefaction wave and the shock, or saturation front, between the upstream displacing fluid and the downstream fluid-in-place. The dashed line represents a normalized tracer profile or the saturation profile that would correspond to a piston-like displacement.

(b) Polymer flooding. This saturation profile shows the rarefaction wave and two shocks: one between the upstream polymer solution and the displaced water, and one between the downstream displaced water and the fluid-in-place. The dashed line represents the normalized mobility reduction which traces polymer.

Fig. 9: Comparison of in-situ water saturation profiles (solid line) along a horizontal line from the injection to the production well for waterflooding and polymer flooding.

Polymer flooding displacement patterns are more complex than for waterflooding and usually exihibit two saturation fronts, as shown by many authors [35,36,9,37] and reported in Fig. 9b. Specifically, one has:

- A first downstream front, denoted S_f^1 in Fig. 9b, that separates the displacing polymer-free water and the initial fluids in place (this front saturation is close but not necessarily the same as for waterflooding),
- A second upstream front, denoted S_f^2 in Fig. 9b, that separates the displacing polymer solution and the displaced polymer-free water.

The upstream polymer saturation front S_f^2 is way larger than the polymer-free downstream saturation front S_f^1 since it accounts for a larger water viscosity due to polymer. As a consequence, the displacement stability is examined at both fronts, as we shall see in Section 3.

3 Characterization of displacement stability

Displacement stability is assessed in the following manner. First, saturation fronts $S_f^{1,2}$ and fluids upstream and downstream mobilities $\lambda_\alpha^\pm = k_{r\alpha}(S_f^\pm)/\mu_\alpha^\pm$ are computed performing one-dimensional Buckley-Leverett calculations and reservoir simulations on the same rock-fluid system and geometry that was previously described in Section 2.2. Numerical simulations are performed with a mesh that accounts for the flow in the x-coordinate only, that is with a one-dimensional discretization such as $\Delta x = 0.5$ m and $\Delta y = L = 150$ m. Then, the hypothetical displacement stability criteria $M_{a,b,c,d}$ given by Eq. (7) are computed. It is worth noting that one-dimensional flow calculations cannot render viscous fingering but capture the displacing saturation fronts that are needed to estimate the upstream and downstream mobilities $\lambda_\alpha^\pm$.

The flow stability is probed in a second step by performing two-dimensional simulations with $\Delta x = \Delta y = 0.5$ m: if the displacement is stable, the displacing front(s) remain sharp and stable all along the x- and y-coordinate, and if the displacement is unstable, fingers initiate and grow. Since the relative permeabilities are assumed to be known with given saturation end points, the viscosity ratio between oil and water μ_w/μ_o is varied by increasing the water viscosity when considering waterflooding or through the polymer mobility reduction function R_m when considering polymer flooding. Eventually, the flow behavior which is observed using two-dimensional simulations, i.e. fingers appearance and growth or not, is linked to the stability criteria candidates $M_{a,b,c,d}$ previously estimated using one-dimensional calculations, that can now be confronted to numerical experiments: if $M \leq 1$ the displacement is stable, and if $M > 1$ the displacement is unstable. Such a coherent picture and stability criterion is looked for amongst the $M_{a,b,c,d}$ descriptors in the next sections when considering waterflooding first, then polymer flooding.

3.1 Impact of viscosity ratio on waterflooding stability

To start with, Fig. 10 reports saturation profiles that were obtained with two-dimensional waterflooding simulations when considering a 1500 cP viscous oil displacement by a 16, 40 and 60 cP viscous water. Clearly, fingers appear and grow for $\mu_w = 16$ cP and $\mu_w = 40$ cP to a lesser extent, whereas the saturation front is sharp and stable for $\mu_w = 60$ cP. Buckley-Leverett calculations and 1D simulations saturation fronts estimates are very close for each case: $S_f = 0.49 - 0.505$, $0.547 - 0.56$ and $0.558 - 586$ for $\mu_w = 16$, 40 and 60 cP and when considering Buckley-Leverett calculation or one-dimensional simulation, respectively. As expected, the larger μ_w, the larger S_f is.

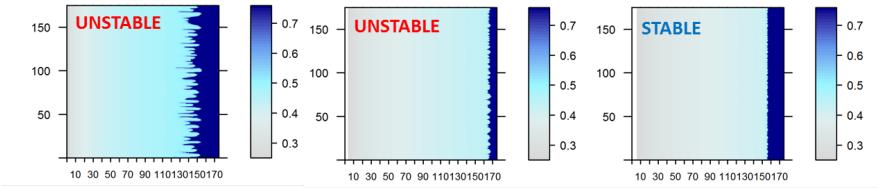

	$t = 30$	BL
S_f	0.49	0.505
M_a	0.96	1.2
M_b	1.28	1.5

	$t = 40$	BL
S_f	0.547	0.56
M_a	0.84	0.99
M_b	1.05	1.18

	$t = 40$	BL
S_f	0.558	0.586
M_a	0.64	0.88
M_b	0.84	1.03

Fig. 10: Waterflooding two-dimensional saturation profiles when simulating a 1500 cP viscous oil displacement by a 16, 40 and 60 cP viscous water, (from left to right, see the text).

When calculating the "rule-of-thumb" mobility ratio M_0 given by Eq. (6) as for an ideal piston-like displacement, one gets $M_0 = 0.2 \times \mu_o/\mu_w$, that is $M_0 = 18.75$, 7.5 and 5 for $\mu_w =$ 16, 40 and 60 cP, respectively. Therefore, one would expect an unstable flow in each case according to this mobility ratio definition, and a stable flow would be obtained for $\mu_w \geq 300$ cP. This is not what we observe in Fig. 10, because flow stability depends on fluids viscosity ratio and saturation front, as previously shown by [38], and the latter is not accounted for by the "rule-of-thumb" mobility ratio M_0 which therefore clearly overestimates the stability threshold.

When calculating the "shock" mobility ratios M_a and M_b given by Eq. (7), one gets $M_a = 0.96$ and $M_b = 1.28$ for the $\mu_w = 16$ cP case which yields an unstable displacement as reported Fig. 10, $M_a = 0.84$ and $M_b = 1.05$ for the $\mu_w = 40$ cP case which exhibits small fingers, and $M_a = 0.64$ and $M_b = 0.84$ for the $\mu_w = 60$ cP case which leads to a stable front. As a consequence, the relevant stability criterion for waterflooding is the mobility ratio M_b, which is defined as the ratio of the total upstream mobility over the total downstream mobility. This result is in line with previous linear stability analysis works [10, 11, 13]. M_a, which is defined as the ratio of the upstream water mobility over the total downstream mobility, tends to overestimate the flow stability. It is worth noting that the mobility ratios computed from Buckley-Leverett calculation underestimate the flow stability compared to 1D simulations, because Buckley-Leverett calculation is free of any numerical diffusion and yields slightly higher saturation fronts values S_f, as reported in Fig. 10.

3.2 Impact of mobility reduction on polymer flooding stability

The same stability analysis is carried out for polymer flooding, which exhibits two saturation fronts. Instead of varying the water viscosity, several mobility reduction R_m (see Section 2.1) of 4, 20, 40 and 100 are considered. In-place water viscosity is 1 cP and polymer does not adsorb on the rock.

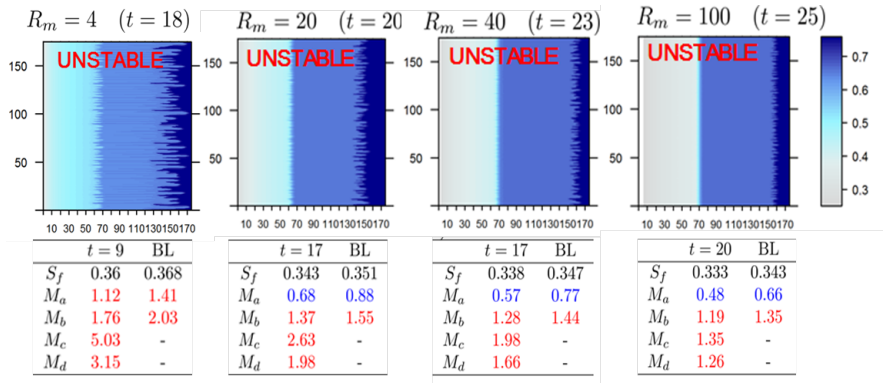

	$t = 9$	BL
S_f	0.36	0.368
M_a	1.12	1.41
M_b	1.76	2.03
M_c	5.03	-
M_d	3.15	-

	$t = 17$	BL
S_f	0.343	0.351
M_a	0.68	0.88
M_b	1.37	1.55
M_c	2.63	-
M_d	1.98	-

	$t = 17$	BL
S_f	0.338	0.347
M_a	0.57	0.77
M_b	1.28	1.44
M_c	1.98	-
M_d	1.66	-

	$t = 20$	BL
S_f	0.333	0.343
M_a	0.48	0.66
M_b	1.19	1.35
M_c	1.35	-
M_d	1.26	-

Fig. 11: Polymer flooding two-dimensional saturation profiles when simulating a 1500 cP viscous oil displacement by a polymer solution of mobility reduction 4, 20, 40 and 100. Stablity analysis is carried out for the polymer-free downstream saturation front S_f^1.

Figures 11 and 12 report saturation profiles that were obtained with 2D polymer flooding simulations. Specifically, Fig. 11 focuses on the polymer-free downstream saturation front S_f^1 whereas Fig. 12 focuses on the polymer upstream saturation front S_f^2. As expected, the larger the mobility reduction R_m, the larger S_f^2 is. While the downstream saturation front S_f^1 is always unstable for all the considered mobility reduction values, the polymer upstream saturation front S_f^2 undergoes a smooth transition from instability, for $R_m = 4$ and 20, to stability for $R_m = 100$, with an intermediate almost stable displacement for $R_m = 40$.

This transition from an unstable to a stable displacement saturation pattern is accounted for by mobility ratios M_a and M_b, but since M_a fails to predict the downstream saturation

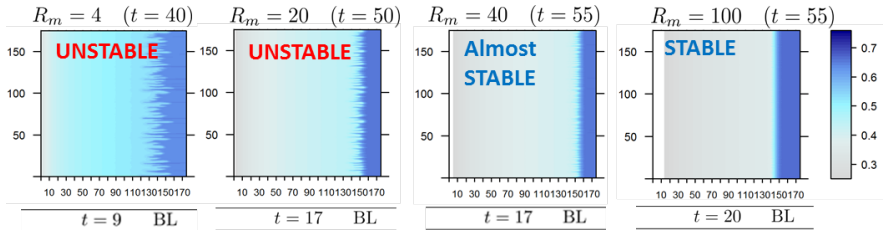

	$t = 9$	BL
S_f	0.457	0.477
M_a	1.33	1.59
M_b	1.47	1.75
M_c	3.66	-
M_d	2.67	-

	$t = 17$	BL
S_f	0.53	0.559
M_a	1.01	1.26
M_b	1.19	1.39
M_b	2.55	-
M_b	2.08	-

	$t = 17$	BL
S_f	0.57	0.598
M_a	0.88	1.04
M_b	1.01	1.13
M_c	1.94	-
M_d	1.67	-

	$t = 20$	BL
S_f	0.62	0.708
M_a	0.66	0.43
M_b	0.74	0.8
M_c	1.24	-
M_d	1.13	-

Fig. 12: Polymer flooding two-dimensional saturation profiles when simulating a 1500 cP viscous oil displacement by a polymer solution of mobility reduction 4, 20, 40 and 100. Stability analysis is carried out for the polymer upstream saturation front S_f^2.

unstable behavior for $R_m = 20$, 40 and 100, only M_b predicts the displacement stability, as previously shown for waterflooding in Section 3.1. Additional simulations considering intermediate mobility reductions values up to 300 have been performed, as depicted in Fig. 14. As a consequence, based on this shock mobility ratio M_b and one-dimensional simulations that define the front saturations S_f^1 and S_f^2, one can predict the flow stability without the need to perform time-consuming high-resolution two-dimensional simulations. Specifically, one can predict the optimal mobility reduction threshold that makes the displacement stable at the upstream saturation front S_f^2. For instance, mobility reduction values larger than 40 yield a stable displacement as shown by Fig. 14 for the considered example.

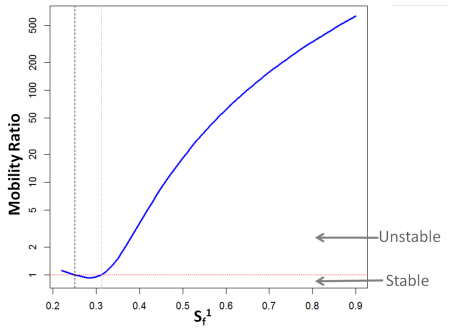

Fig. 13: Polymer flooding downstream mobility ratio M_b as a function of the polymer-free downstream saturation S_f^1 front (dotted line represents the stability threshold).

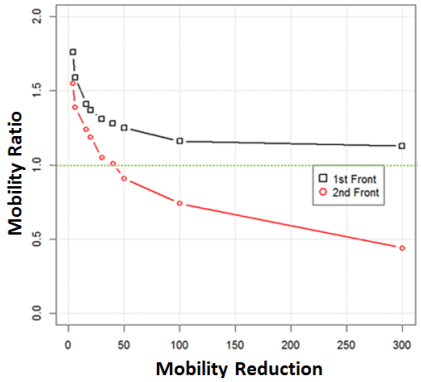

Fig. 14: Polymer flooding downstream (for $S_w = S_f^1$) and upstream (for $S_w = S_f^2$) mobility ratios M_b as a function of the mobility reduction (dotted line represents the stability threshold).

Figures 15 and 16 report the fingers dynamical evolution for the downstream and upstream saturation fronts in terms of fingers spreading and number as a function of time before water or polymer breathrough. While the fingers number decreases linearly with time

as small fingers merge into larger ones, their spreading linearly increases with time, approximately. In addition, fingers number decline and spreading growth are inversely proportional to the mobility reduction. This behavior is in line with previous observations obtained for fairly homogeneous porous media [17,16,39,28].

Fig. 17 compares the time evolution of the most advanced fingertip position for the dowstream and upstream saturation fronts, obtained from two-dimensional polymer flooding simulation when varying the mobility reduction. It shows that the most advanced fingertip velocity is constant for all the considered mobility reduction values.

As expected, the polymer-free downstream front fingers spreading grows faster than the polymer upstream one that develops a larger mobility ratio, as shown by Fig. 18 which compares the water and polymer breakthrough times t_b^1 and t_b^2 through the time lag $t_b^2 - t_b^1$ as a function of the mobility reduction. Time lag $t_b^2 - t_b^1$ increases for non-optimal mobility reductions yielding unstable displacements.

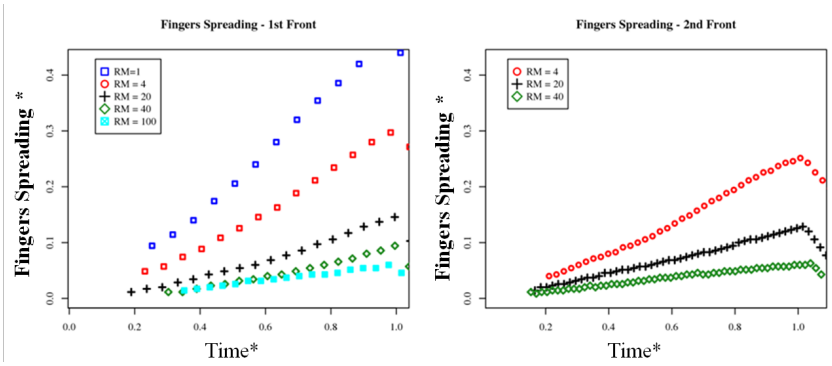

Fig. 15: Time evolution of fingers spreading for the downstream (left figure) and upstream (right figure) saturation fronts, before water or polymer breakthrough, obtained from two-dimensional polymer flooding simulation when varying the mobility reduction

3.3 Impact of polymer adsorption on polymer flooding stability

We now consider polymer adsorbs instantaneously and irreversibly on the rock. The mass conservation equation (1) involve the local and time-dependent adsorbed polymer mass fraction on the rock C_r^p which is computed from an equilibrium between rock and polymer solution that transports the mobile polymer mass fraction C_w^p. This equilibrium is driven by an adsorption function $\mathscr{A}$ which may depend on C_w^p and yields the adsorbed polymer mass per mass of rock (see [25] for more details). Irreversible and instantaneous polymer adsorption is modeled by setting $\mathscr{A} = A_0$ where A_0 is a positive constant and denotes the rock adsorption capacity.

Polymer flooding stability analysis is performed again considering a rock adsorption capacity of 50 μg/g. As reported in Figures 19a, 19b, 20 and 21, the flow stability at both upstream and downstream saturation fronts is again predicted by the shock mobility ratio M_b only. Polymer adsorption delays the polymer upstream saturation front S_f^2 and leads to:

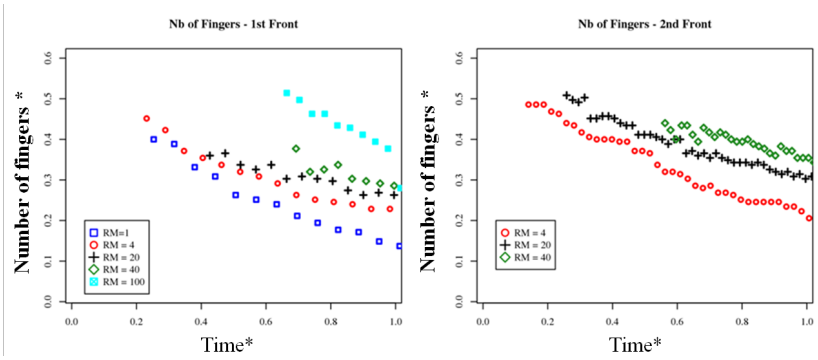

Fig. 16: Time evolution of fingers number for the downstream (left figure) and upstream (right figure) saturation fronts, before water or polymer breakthrough, obtained from two-dimensional polymer flooding simulation when varying the mobility reduction.

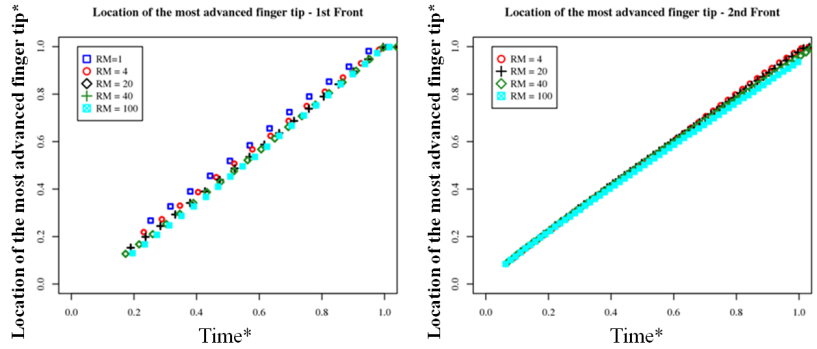

Fig. 17: Time evolution of the most advanced fingertip position for the downstream (left figure) and upstream (right figure) saturation fronts, before water or polymer breakthrough, obtained from two-dimensional polymer flooding simulation when varying the mobility reduction.

- A more unstable downstream front, which is due to the downstream saturation front S_f^1 increase when polymer adsorbs. This leads to an increase of $k_{rw}(S_f^1)$ which is not balanced by the decrease of $k_{ro}(S_f^1)$ due to the relative permeabilities setting. Thus $(\lambda_w + \lambda_o)^-$ hence the mobility ratio M_b is larger for the polymer-free downstream saturation front when considering polymer adsorption, as reported in Fig. 19a.
- A more stable polymer upstream saturation front, because $(\lambda_w + \lambda_o)^-$ does not vary significantly when S_f^2 increases whereas $(\lambda_w + \lambda_o)^+$ increases significantly as previously explained. Thus, the mobility ratio M_b is slightly lower when polymer adsorbs on the rock, as reported in Fig. 19a.

These observations still hold when considering rock adsorption capacity values up to 200 μg/g, as shown in Fig. 19b. Hence, the larger polymer adsorption, the more stable the polymer upstream saturation front is and the more unstable the polymer-free downstream saturation front is.

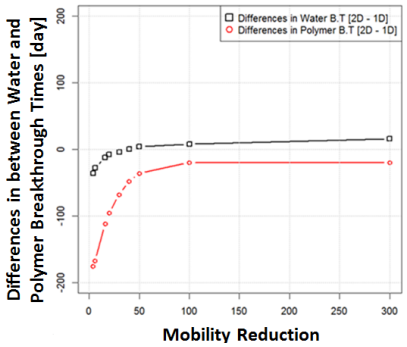

Fig. 18: Comparison of water and polymer breakthrough times t_b^1 and t_b^2, through the time lag $t_b^2 - t_b^1$, obtained from one- and two-dimensional polymer flooding simulations as a function of the mobility reduction. Time lag $t_b^2 - t_b^1$ increases for non-optimal mobility reductions yielding unstable displacements.

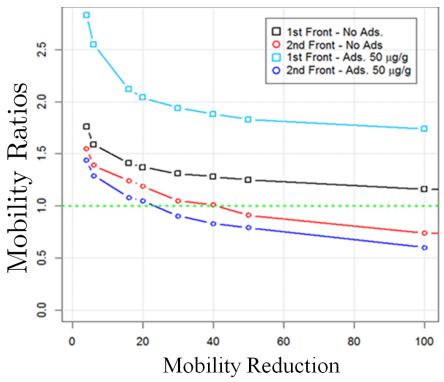

(a) Comparison of upstream and downstream mobility ratios M_b as a function of mobility reduction R_m with and without polymer adsorption.

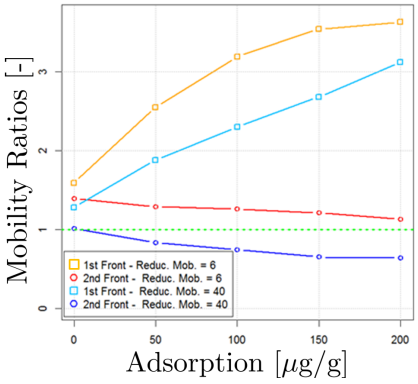

(b) Comparison of upstream and downstream mobility ratios M_b as a function of rock adsorption capacity for $R_m = 6$ and 40.

Fig. 19: Comparison of upstream and downstream mobility ratios M_b as a function of rock adsorption capacity and polymer mobility reduction (green dotted line represents the stability threshold).

As a consequence, when polymer adsorption is known, one can determine the optimal mobility reduction threshold that stabilizes the polymer upstream front with $M_b = 1$. For instance, such an optimal mobility reduction would be 40, 22 and 6 when polymer rock adsorption capacity is 0, 50 and 250 μg/g, respectively, as reported in Fig. 21.

3.4 Impact of polymer degradation on polymer flooding stability

To finish with homogeneous porous media, we now probe the impact of polymer degradation on displacement stability. To do so, we adopt a simplified approach by assuming the polymer degradates with time and leads to a mobility reduction exponential decay that reads $R_m(t) =$

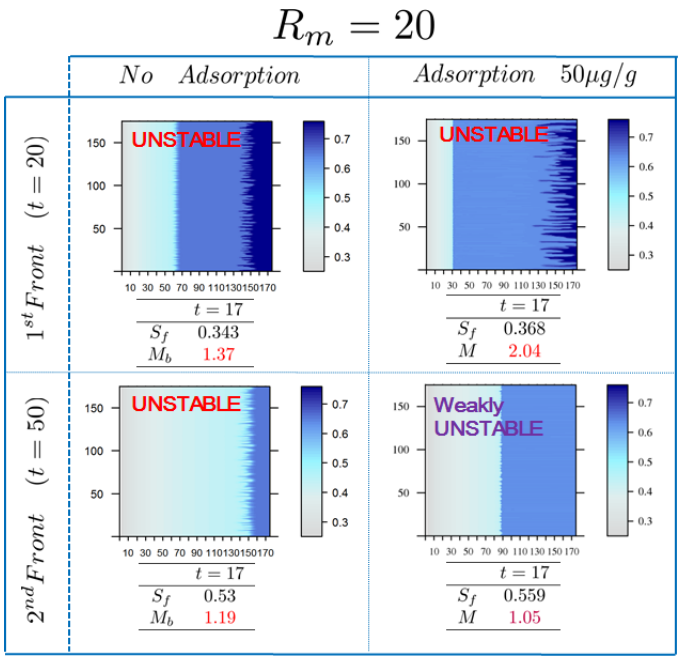

Fig. 20: Comparison of upstream and downstream saturation maps with and without polymer adsorption with a mobility reduction of 20 and a rock adsorption capacity of 50 μg/g.

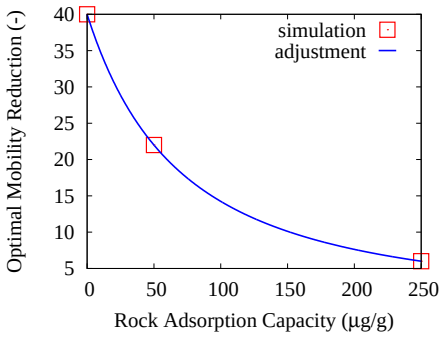

Fig. 21: Optimal mobility reduction leading to a stable displacement such as $M_b = 1$ as a function of polymer rock adsorption capacity.

$R_0\,\mathrm{e}^{-t/\tau}$, where R_0 denotes the non-degradated-polymer mobility reduction and τ a time constant. If, in addition, we assume the polymer velocity to be constant, which is a fair approximation in our example, the mobility reduction time evolution can be converted into a simple spatial dependency that reads $R_m(t) = R_m(x) = R_0\,\mathrm{e}^{-x/\zeta}$ where $R_0 = R_m(x=0)$ for all $0 \leq y \leq L$. The characteristic lengthscale ζ can be eleminated by constraining the mobility reduction value to be equal to R_0/a at location x_a with $0 \leq x_a \leq L$ and $a \geq 1$, which yields $R_m(x) = R_0\,a^{-x/x_a}$. Hereafter, we study the impact of a non-degradated-polymer mobility reduction R_0 of 40 that degradates into a mobility reduction value of 4 at $x = L$ for all

$0 \leq y \leq L$ by setting $x_a = L$ and $a = 10$, that is $R_m(x) = R_0 \times 10^{-x/L}$ for all $0 \leq y \leq L$. Polymer does not adsorb on the rock.

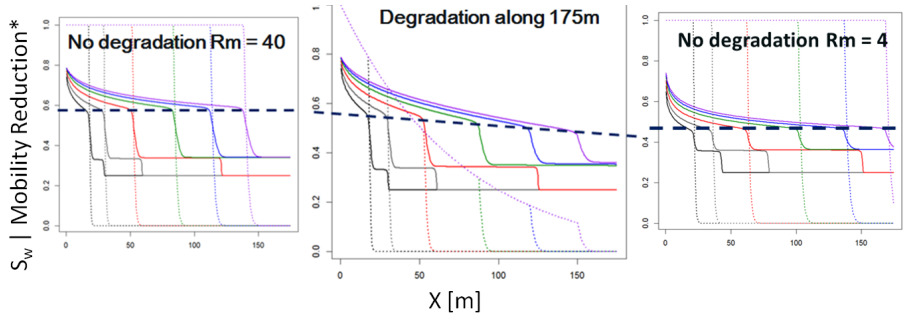

Fig. 22: Comparison of saturation profiles (solid lines) and normalized mobility reduction profiles (dotted lines), with and without polymer degradation, along a horizontal line between injection and production wells. Left figure: $R_m = 40$ without degradation; center figure: polymer degradation such as $R_m(x) = R_0 \times 10^{-x/L}$ (see the text); right figure: $R_m = 4$ without degradation (colors correspond to different times).

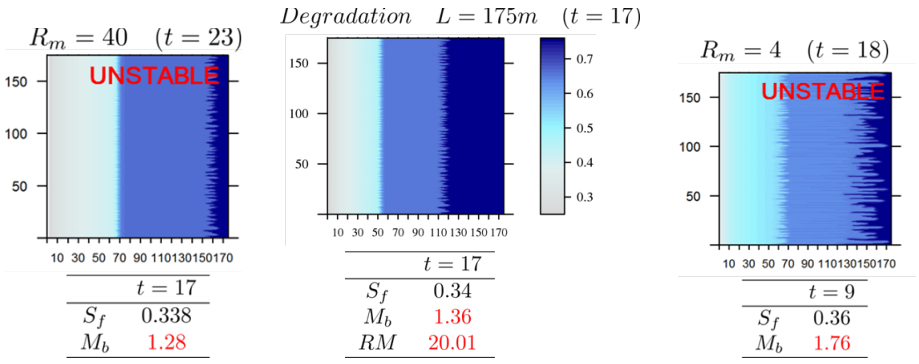

Fig. 23: Comparison of two-dimensional polymer-free downstream saturation front S_f^1 profiles with and without polymer degradation. Left figure: $R_m = 40$ without degradation; center figure: polymer degradation such as $R_m(x) = R_0 \times 10^{-x/L}$ (see the text); right figure: $R_m = 4$ without degradation.

Polymer degradation leads to a continuously changing mobility reduction. Therefore, the upstream and downstream saturation fronts are no longer invariant as shown in Figures 22 and 24. Specifically, because the mobility reduction follows an exponential decay between the injection and production wells, the polymer upstream saturation front consinuously decreases when travelling through the porous medium while the polymer-free downstream saturation front increases. As a consequence, the mobility ratio varies with time, as reported in Fig. 24.

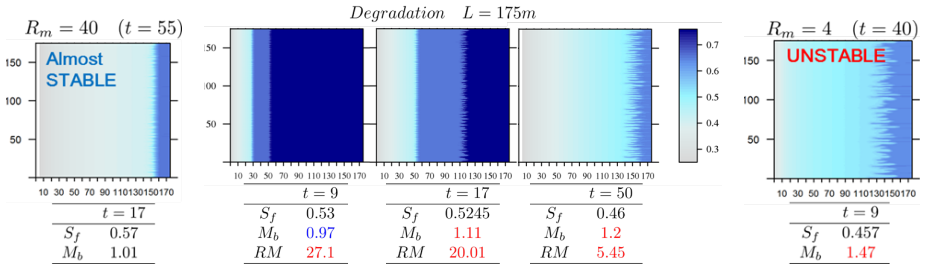

Fig. 24: Comparison of two-dimensional polymer upstream saturation front S_f^2 profiles with and without polymer degradation. Left figure: $R_m = 40$ without degradation; center figure: polymer degradation such as $R_m(x) = R_0 \times 10^{-x/L}$ (see the text); right figure: $R_m = 4$ without degradation.

Table 3: Permeability heterogeneity Dykstra-Parsons coefficients and standard deviations.

Model label	Dykstra-Parsons coefficient V_{DP} (-)	Permeability standard deviation σ_k (mD)
V_{DP}^1	0.1	422.6
V_{DP}^2	0.5	3 141
V_{DP}^3	0.8	14 048

As for waterflooding and polymer flooding with or without adsorption, the shock mobility ratio M_b proved to be the only stability criterion in agreement with two-dimensional simulations when polymer degradates. However, the dependency of the polymer upstream saturation front S_f^2 in the mobility reduction is not the same whether polymer degradates or not: the flow is more unstable when polymer degradates.

4 Interaction between viscous fingering and channeling in heterogeneous porous media

4.1 Heterogeneity modelling

In order to assess the coupling of viscous fingering with heterogeneity, we consider nine two-dimensional x-y heterogeneous permeability distributions, as reported in Fig. 25. Porosity is constant ($\Phi = 0.35$). Permeability distribution is log-normal with a mean of 4 D. Three standard deviations of 422.6, 3 141 and 14 048 D are considered. They correspond to three Dykstra-Parsons coefficients [2] [40] V_{DP} of 0.1, 0.5 and 0.8 as reported in Table 3.

Permeability spatial distribution is driven by a spherical variogram whose correlations lengths in the x- and y-coordinate are denoted ξ_x and ξ_y. We consider three correlation lengths ξ_x of 17.5, 87.5 and 157.5 m, as reported in Table 4, with $\xi_y = \xi_x/10$. Thus we consider three dimensionless correlation lengths CL of 0.1, 0.5 and 0.8, defined as the correlation length in the x-coordinate divided by the domain length L of 175 m.

[2] For a log-normal random variable of parameters m and σ, the Dykstra-Parsons coefficient is defined as $V_{\mathrm{DP}} = \frac{e^m - e^{m-\sigma}}{e^m} = 1 - e^{-\sigma}$, which rewrites $\sigma = -\log(1 - V_{\mathrm{DP}})$.

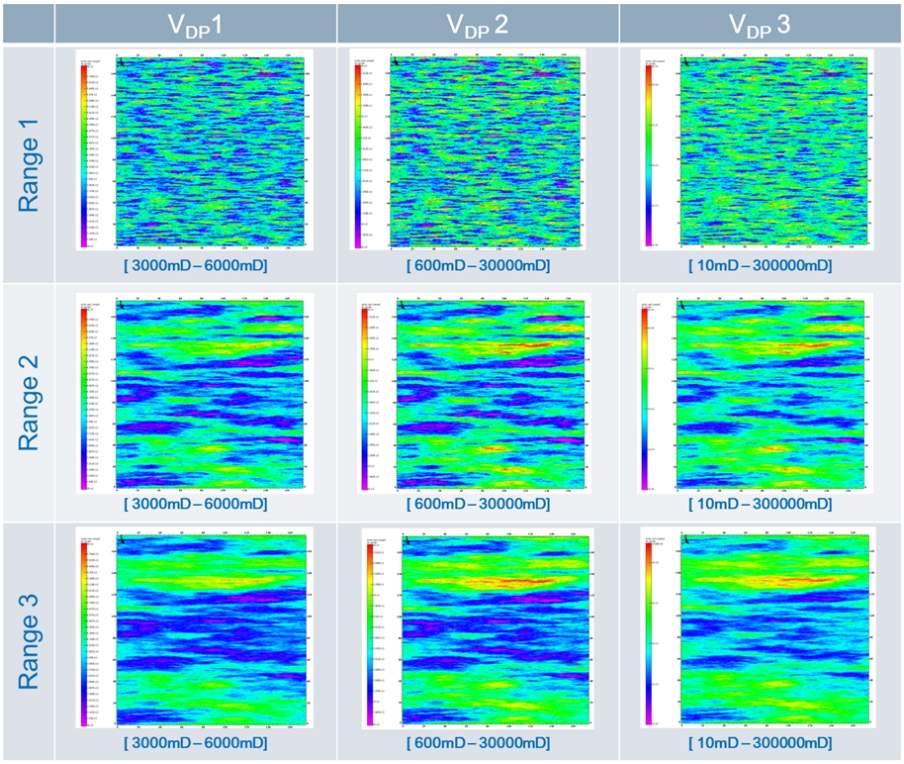

Fig. 25: Permeability fields for different ranges and variances. Dykstra-Parsons coefficients V_{DP} and dimensionless correlation lengths (denoted "range" in the figure) numbering is given in Tables 3 and 4.

Table 4: Permeability heterogeneity correlation length.

Model label	Dimensionless correlation length CL (-)	Correlation length in the x-coordinate ξ_x (m)
CL_1	0.1	17.5
CL_2	0.5	87.5
CL_3	0.8	157.5

4.2 Impact of heterogeneity on polymer flooding stability

Thirty configurations are generated by combining mobility reduction, permeability Dykstra-Parsons coefficient and dimensionless correlation length values. Polymer does not adsorb on the rock nor degradates. These combinations $(R_m, V_{\mathrm{DP}}, CL)$ are generated from:

- Three mobility reduction values of 1, 20 and 100,
- Four Dykstra-Parsons coefficients of 0, 0.1, 0.5 and 0.8,
- Four dimensionless correlations lengths of 0, 0.1, 0.5. and 0.9.

Figures 26 and 27 compare the saturation profiles as a function of nine (V_{DP}, CL) combinations for waterflooding when water breakthrough is obtained and after one pore volume of water has been injected, respectively and do the same for polymer flooding, with a mobility

Table 5: Polymer breakthrough times function of nine (V_{DP}, CL) combinations (see figure 25) and mobility ratio value.

Polymer flooding with $R_m = 20$		
0.43 PV	0.28 PV	0.18 PV
0.37 PV	0.15 PV	0.08 PV
0.36 PV	0.12 PV	0.06 PV
Polymer flooding with $R_m = 100$		
0.58 PV	0.40 PV	0.26 PV
0.54 PV	0.24 PV	0.12 PV
0.51 PV	0.2 PV	0.1 PV

reduction of 20 and 100. We compare the polymer upstream and polymer-free downstream saturation profiles at water breakthrough, and after one pore volume of water has been injected. Similar figures can be drawn when polymer breakthrough is obtained (not shown here). Polymer breakthrough times function of nine (V_{DP}, CL) combinations are summarized in Table 5.

The following observations can be drawn:

- Water and polymer breakthrough times decrease when increasing heterogeneity for all mobility reduction values.
- A large enough heterogeneity leads to by-pass and unswept areas whereas all the reservoir is swept in the homogeneous cases after one injected pore volume, as shown in Figures 27 (right columns).
- By-pass is more pronounced when viscous fingering and channeling occur (see bottom right panel of Figures 27) than when only channeling occurs. This low sweep efficiency is due to the coupling of viscous fingering and channeling.

4.3 Fingers dynamical behavior analysis

It is worth noting that the upstream saturation front is stable when considering a mobility reduction of 100. Hence no viscous fingering occurs and only channeling remains. Therefore, this case will serve as a reference for quantifying the coupling between viscous fingering and heterogeneity.

Figures 28a, 28b and 28c compare the time evolution of fingers spreading, number and most advanced fingertip position for the downstream and upstream saturation fronts, before water or polymer breakthrough, obtained from two-dimensional polymer flooding simulations with $R_m = 1$, 20, 100 when varying heterogeneity drivers V_{DP} and CL as previously explained in Section 4.2. The following observations can be drawn:

- For low Dykstra-Parsons coefficients, the flow behavior is dominated by viscous fingering with a similar dynamical behavior as for when considering a homogeneous porous medium, as reported in Section 3.2. On the contrary, for large V_{DP} values (for $V_{DP} \geq 0.5$), fingers number no longer decreases linearly with time but remains approximately constant, because of channeling which is caused by heterogeneity. In addition, fingers number does not depend on mobility reduction anymore but remains approximately constant for all mobility reduction values.
- The velocity of the most advanced finger and the fingers spreading are larger compared to the homogeneous case, and fingers spreading no longer grows linearly with time.

Indeed, the frontal advance is constrained by flow barriers that lead to preferential pathways. As a consequence, the areal sweep efficiency decreases and leads to early breakthrough times as well as very late and slowed down upstream saturation tails.
- Specifically, the upstream saturation tails behave very particularly for low correlation lengths: while low-permeability lenses (colored in black in Fig. 26) are by-passed and lead to a large spreading of fingers at early times, the fingers spreading decreases very significantly at late times when these lenses have been swept eventually. Hence the fingers spreading piecewise linear time evolution for low *CL* values that is reported in Fig. 28b.
- Largest fingers spreading is obtained with lower mobility reductions that lead to unstable flow. The more unstable the flow, the more sensitive it is to heterogeneities, which results in a more pronounced by-pass due to the coupling of viscous fingering and heterogeneity.

4.4 Oil recovery analysis

The decrease in sweep efficiency previously described in Sections 4.2 and 4.3 is also observed on the produced cumulative oil volume as a function of time (expressed as a fraction of the initial oil in place volume), as reported in Fig. 29. Sweep efficiency and oil production decrease is more pronounced when combining large heterogeneities and viscous fingering. It is worth noting that the classical [36] polymer flooding two-slope oil production curve, that results from the polymer upstream and polymer-free downstream saturation fronts, is smoothed out by channeling as reported in Fig. 29. In practice, this signature can be used to infer channeling when production well data are available.

Still, polymer flooding remains more interesting than waterflooding even for highly heterogeneous media. Indeed, even when strong channeling occurs, polymer flooding recovery efficiency is larger than for a waterflooded homogeneous medium, as shown in Fig. 29 (dotted orange and black lines).

4.5 Breakthrough time analysis

Figures 30a and 30b compare polymer breakthrough time as a function of mobility reduction and permeability heterogeneity drivers (Dykstra-Parsons coefficient V_{DP} and correlation length *CL*). When considering large heterogeneity drivers for $V_{\mathrm{DP}} \geq 0.5$ and $CL \geq 0.5$, polymer breakthrough times get closer and closer and tend to be similar for all mobility reduction values. This constitutes a signature of the predominance of channeling over viscous fingering.

Figure 31 compare polymer and water breakthrough times difference (expressed in injected pore volume) as a function of mobility reduction and permeability heterogeneity drivers. Results are highly dispersed for low V_{DP} values, which is the signature of a viscous-fingering-dominated flow. However, for a very unstable flow (here, at low R_m), results vary with the correlation length *CL* because of the interaction between viscous fingering and heterogeneities. Thus, the delay between polymer and water arrival times is more sensitive to the heterogeneity if the flow is unstable. On the contrary, for $V_{\mathrm{DP}} = 0.8$ and $CL \geq 0.5$, the difference between polymer and water breakthrough times are nearly the same for all viscous conditions, which is a signature of a channeling-dominated flow.

Figures 32 and 33 report the polymer breakthrough time and polymer and water breakthrough times difference as a function of permeability heterogeneity drivers. This concise mapping

- Sums up the main sensitivity to the Dykstra-Parsons coefficient V_{DP}, to the correlation length for $CL \leq 0.5$, and highlights a very contrasted behavior for low V_{DP} values when varying the mobility reduction.
- Identify the channeling- and viscous fingering-dominated flow regimes as a function of the porous medium permeability heterogeneity drivers.

5 Conclusions

A new hydrodynamical stability criterion, based on previous linear stability analysis results obtained for immiscible oil displacement by water, has been proposed and tested for polymer-based immiscible displacements. High-resolution numerical experiments at pilot scale have been performed within a heavy oil context. They were designed with a bias-free perturbation scheme that triggers viscous fingering when unstable flow conditions are met. The development of viscous fingering in homogeneous porous media is driven by the shock mobility ratio defined as the ratio of the total fluids upstream mobility over the total fluids downstream mobility. This stability criterion proved to predict both the polymer upstream and polymer-free downstream saturation fronts stability, that are typical of a polymer displacement, whether polymer adsorbs on the rock or degradates, or not. Suprisingly, polymer adsorption improves the flow stability while polymer degradation, that leads to continuously changing mobilities, makes the flow more unstable.

Other stability criteria have been proposed and tested but failed to predict the displacement stability, among which the "rule-of-thumb" mobility ratio which assumes the displacement to be piston-like, discards any saturation dependency and way underestimates the displacement stability threshold. In this specific context, fingers dynamical behavior has shown to be in line with previous works addressing single phase miscible flow or immiscible oil displacement by water in porous media. Indeed, time evolution of fingers spreading and number is linear: fingers transversally merge while growing in the flow direction. These results may prove to be useful in practice when considering heavy oil displacements by polymer solutions, whose design is sometimes tricky with respect to the required mobility reduction that may cancel viscous fingering. This work shows how to quantitatively design such a stable displacements in fairly homogeneous porous media whether polymer adsorbs on the rock or degradates, or not.

Investigation on porous media of variable heterogeneity distributions has shown how viscous fingering couples with heterogeneity and leads to even more marked, distorded and unstable flow patterns, that are not solely driven by the porous medium heterogeneity. The more unstable the flow is, the more sensitive it is to heterogeneity. In-depth fingers dynamical behavior analysis has shown a very specific time evolution behavior that is quite different from viscous fingering in fairly homogeneous two-dimensional porous media. In addition, we have shown how such a flow pattern is related with production data such as water and polymer breakthrough times and/or oil recovery profiles as a function of time, which can be used in turn to infer displacement stability and porous medium heterogeneity features.

To conclude, we dispose of a robust procedure to predict, analyze and model polymer-based heavy oil displacements stability. Such an identification of the dominant flow mechanisms constitutes a valuable knowledge basis for developping a proper upscaling method-

ology when viscous fingering occurs [14]. It is worth noting such results hold for two-dimensional Hele-Shaw-type flows only. The lack of experimental data addressing specifically the stability of polymer-based displacements in porous media does not allow us to draw a definitive conclusion regarding the validity of the proposed stability criterion. To this regard, demonstrative polymer-based displacement experiments in homogeneous permeable core plugs that are not impacted by lengthscale issues would constitute a very nice step forward. Notwithstanding, the methodology and physical relationships developed herein should be helpful for the assessment and selection of a polymer-based process for improved oil recovery purposes.

Acknowledgements

The authors thank A. M. Zadeh (Equinor), V. Kippe (Equinor), B. Robøl (Equinor) and B. Nœtinger (IFP Energies nouvelles) for useful discussions.

References

1. P. G. Saffman and G. Taylor. The penetration of a fluid into a porous medium or Hele-Shaw cell containing a more viscous liquid. Proceedings of the Royal Society of London A: Mathematical, Physical and Engineering Sciences, 245(1242):312–329, 1958.
2. R. L. Chuoke, P. van Meurs, and C. van der Poel. The instability of slow, immiscible, viscous liquid-liquid displacements in permeable media. Petroleum Transactions, AIME, 216:188–194, 1959.
3. G. M. Homsy. Viscous fingering in porous media. Annual Review of Fluid Mechanics, 19(1):271–311, 1987.
4. P. Corlay, P. Lemouzy, , R. Eschard, and L. R. Zhang. Fully integrated reservoir study and numerical forecast simulations of two-polymer pilots in Daqing field. In International Meeting on Petroleum Engineering, pages 331–340. Society of Petroleum Engineers, 1992.
5. E. Delamaide, S. Ha, Y. Hao, X. Jian, D. Wang, and Z. Ye. Results of two polymer flooding pilots in the central area of Daqing oil field. In 68th Annual Technical Conference and Exhibition of The Society of Petroleum Engineers, pages 299–308. Society of Petroleum Engineers, 1993.
6. P. Corlay, E. Delamaide, and D. Wang. Daqing oil field: the success of two pilots initiates first extension of polymer injection in a giant oil field. pages 401–410. Society of Petroleum Engineers, 1994.
7. P. Delaplace, E. Delamaide, F. Roggero, and G. Renard. History matching of a successful polymer flood pilot in the Pelican Lake heavy oil field (Canada). In SPE Annual Technical Conference and Exhibition. Society of Petroleum Engineers, 2013.
8. E. Delamaide, A. Zaitoun, G. Renard, and R. Tabary. Pelican Lake field: first successful application of polymer flooding in a heavy-oil reservoir. SPE Reservoir Evaluation & Engineering, 17:340–354, 2014.
9. P. Daripa, J. Glimm, B. Lindquist, and O. McBryan. Polymer floods: a case study of nonlinear wave analysis and of instability control in tertiary oil recovery. SIAM Journal on Applied Mathematics, 48(2):353–373, 1988.
10. J. Hagoort. Displacement stability of water drives in water-wet connate-water-bearing reservoirs. SPE Journal, 14(1):63–74, 1974.
11. Y. C. Yortsos and A. B. Huang. Linear-stability analysis of immiscible displacement: part 1 – simple basic flow profiles. SPE Reservoir Engineering, 1(4):378–390, 1986.
12. A. J. Chorin. The instability of fronts in a porous medium. Communications in Mathematical Physics, 91(1):103–116, 1983.
13. V. Artus, B. Nœtinger, and L. Ricard. Dynamics of the water-oil front for two-phase, immiscible flow in heterogeneous porous media. 1 – Stratified media. Transport in Porous Media, 56(3):283–303, 2004.
14. H. Luo, M. Delshad, G. A. Pope, and K. K. Mohanty. Interactions between viscous fingering and channeling for unstable water/polymer floods in heavy oil reservoirs. In SPE Reservoir Simulation Conference. Society of Petroleum Engineers, 2017.
15. E. J. Koval. A method for predicting the performance of unstable miscible displacement in heterogeneous media. SPE Journal, 3(2):145–154, 1963.
16. J. R. Waggoner, J. L. Castillo, and L. W. Lake. Simulation of EOR processes in stochastically generated permeable media. SPE Formation Evaluation, pages 173–180, 1992.

17. K. S. Sorbie, F. Feghi, G. E. Pickup, P. S. Ringrose, and J. L. Jensen. Flow regimes in miscible displacements in heterogeneous correlated random fields. SPE Advanced Technology Series, 2(2):78–87, 1994.
18. U. G. Araktingi and F. M. Orr Jr. Viscous fingering in heterogeneous porous media. SPE Advanced Technology Series, 1(1):71–80, 1993.
19. J. Lecourtier, R. Rivenq, P. Delaplace, P. Lemonnier, J. P. Hagry, and D. Lefevre. An innovative polymer flooding simulator based on advanced concepts in polymer physics. In SPE/DOE Enhanced Oil Recovery Symposium. Society of Petroleum Engineers, 1992.
20. D. W. Peaceman. Fundamentals of numerical reservoir simulation. Elsevier, 1977.
21. J. A. Trangenstein and J. B. Bell. Mathematical structure of the black-oil model for petroleum reservoir simulation. SIAM Journal on Applied Mathematics, 49(3):749–783, 1989.
22. L. W. Lake. Enhanced oil recovery. Prentice Hall, 1989.
23. D. W. Green and G. P. Willhite. Enhanced oil recovery. Society of Petroleum Engineers, 1998.
24. C. Marle. Multiphase flow in porous media. Editions Technip, 1981.
25. B. Braconnier, E. Flauraud, and Q. L. Nguyen. Efficient scheme for chemical flooding simulation. Oil & Gas Science and Technology, 69(4):585–601, 2014.
26. D. Bensimon, L. P. Kadanoff, S. Liang, B. I. Shraiman, and C. Tang. Viscous flow in two dimensions. Reviews of Modern Physics, 58(4), 1986.
27. J. Li and B. Rivière. Numerical modeling of miscible viscous fingering instabilities by high-order methods. Transport in Porous Media, 113(3):607–628, 2016.
28. A. Riaz and H. A. Tchelepi. Numerical simulation of immiscible two-phase flow in porous media. Physics of Fluids, 18(1), 2006.
29. A. Adam, D. Pavlidis, J. R. Percival, P. Salinas, R. de Loubens, C. C. Pain, A. H. Muggeridge, and M. D. Jackson. Dynamic mesh adaptivity for immiscible viscous fingering. In SPE Reservoir Simulation Conference. Society of Petroleum Engineers, 2017.
30. R. de Loubens, G. Vaillant, M. Regaieg, J. Yang, A. Moncorgé, C. Fabbri, and G. Darche. Numerical modeling of unstable waterfloods and tertiary polymer floods into highly viscous oils. SPE Journal, 23(5), 2018.
31. R. H. Brooks and A. T. Corey. Properties of porous media affecting fluid flow. Journal of the Irrigation and Drainage Division, 92(2):61–90, 1966.
32. J. W. Amyx, D. M. Bass, and R. L. Whiting. Petroleum reservoir engineering: physical properties. McGraw-Hill, 1960.
33. F. F. Craig. The reservoir engineering aspects of waterflooding. Society of Petroleum Engineers, 1993.
34. G. P. Willhite. Waterflooding. Society of Petroleum Engineers, 1986.
35. E. L. Claridge and P. L. Bondor. A graphical method for calculating linear displacements with mass transfer and continuously changing mobilities. SPE Journal, 14(6):609–618, Dec. 1974.
36. G. A. Pope. The application of fractional flow theory to enhanced oil recovery. SPE Journal, 20(3):191–205, 1980.
37. K. S. Sorbie. Polymer-improved oil recovery. Springer, 2013.
38. A. Riaz and H. A. Tchelepi. Influence of relative permeability on the stability characteristics of immiscible flow in porous media. Transport in Porous Media, 64(3):315–338, 2006.
39. G. Løvoll, Y. Méheust, R. Toussaint, J. Schmittbuhl, and K. J. Måløy. Growth activity during fingering in a porous Hele-Shaw cell. Physical Review E, 70(026301), 2004.
40. H. Dykstra and R. L. Parsons. The prediction of oil recovery by waterflood. Secondary Recovery of Oil in The United States, 2:160–174, 1950.

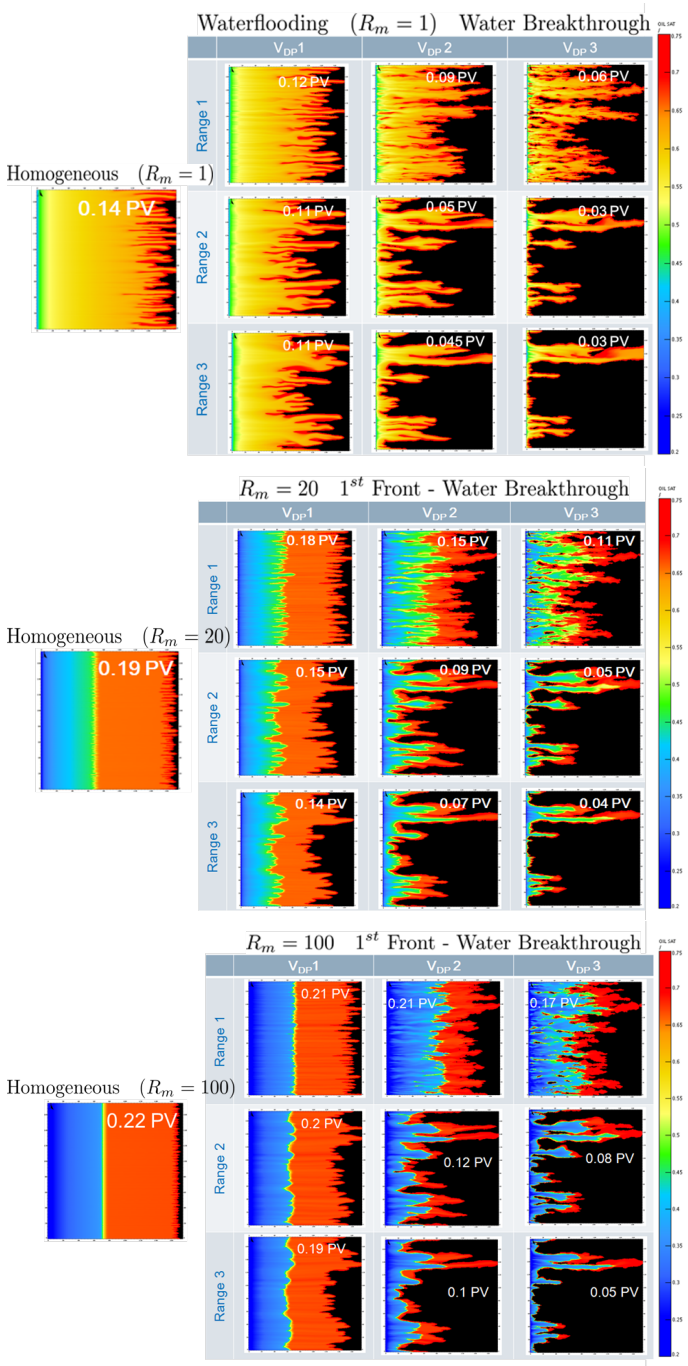

Fig. 26: Comparison of waterflooding saturation profiles (top), polymer flooding downstream and upstream saturation profiles with $R_m = 20$ (middle), polymer flooding downstream and upstream saturation profiles with $R_m = 100$ (bottom) when water breakthrough is obtained as a function of nine (V_{DP}, CL) combinations (see Table 4). Water breakthrough times expressed in injected pore volume are reported in each figure; unswept areas are black.

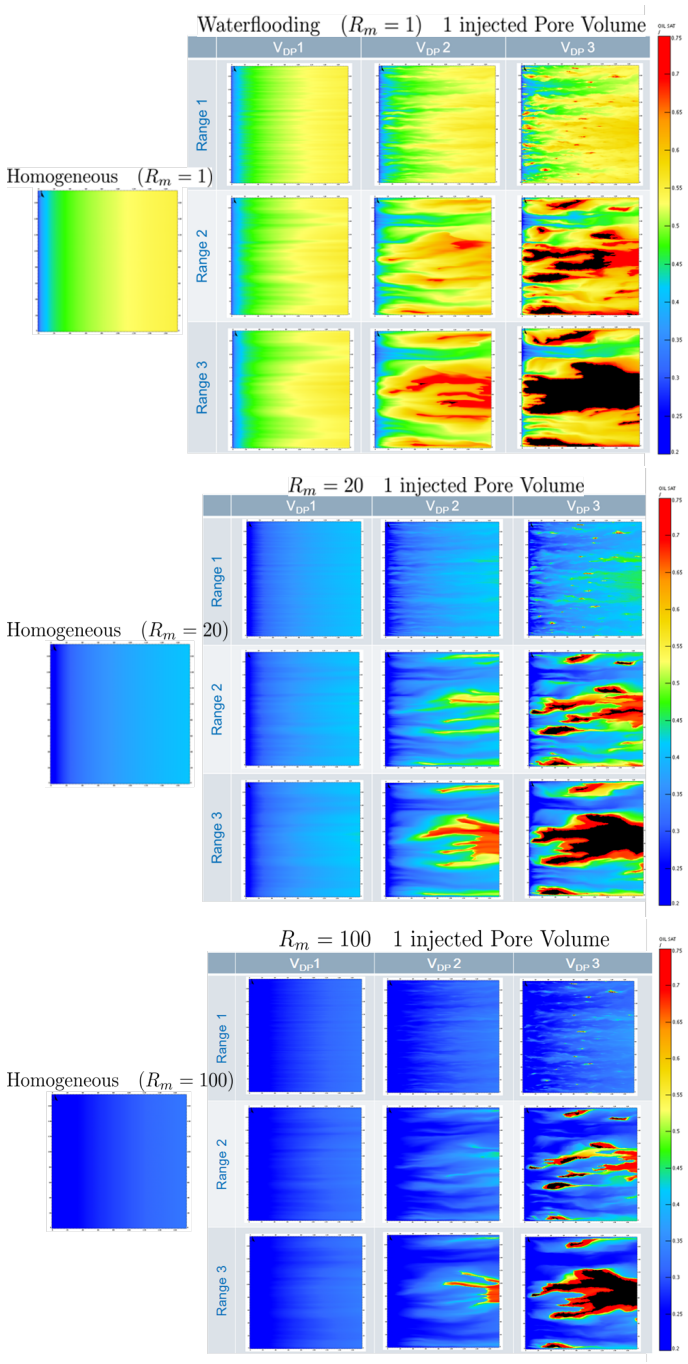

Fig. 27: Comparison of waterflooding saturation (top), polymer flooding saturation with $R_m = 20$ (middle), polymer flooding saturation with $R_m = 100$ (bottom) after one injected pore volume of water has been injected as a function of nine (V_{DP}, CL) combinations (see Table 4). Unswept areas are black.

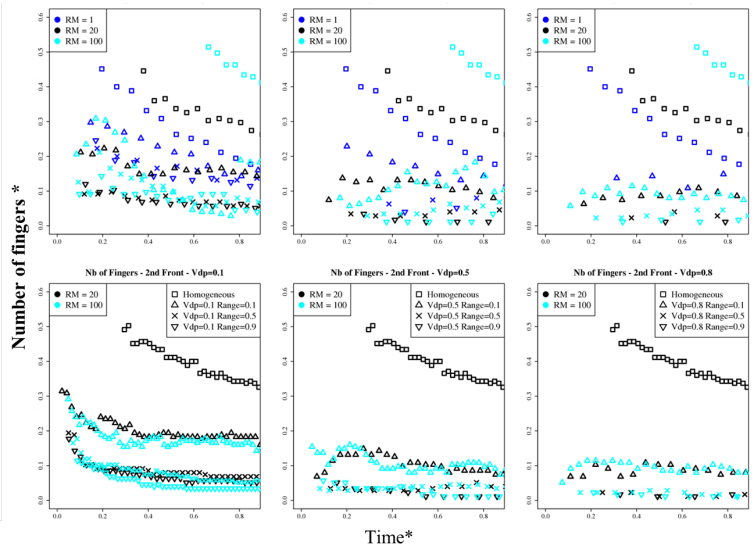

(a) Time evolution of fingers number

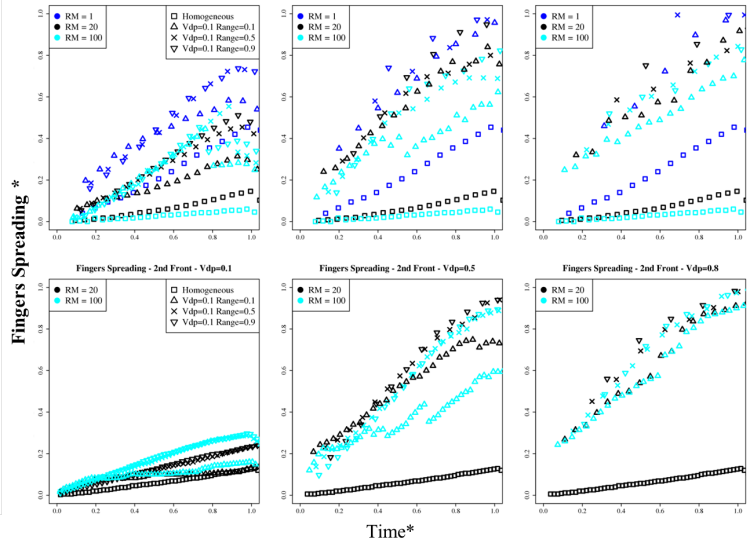

(b) Time evolution of fingers spreading

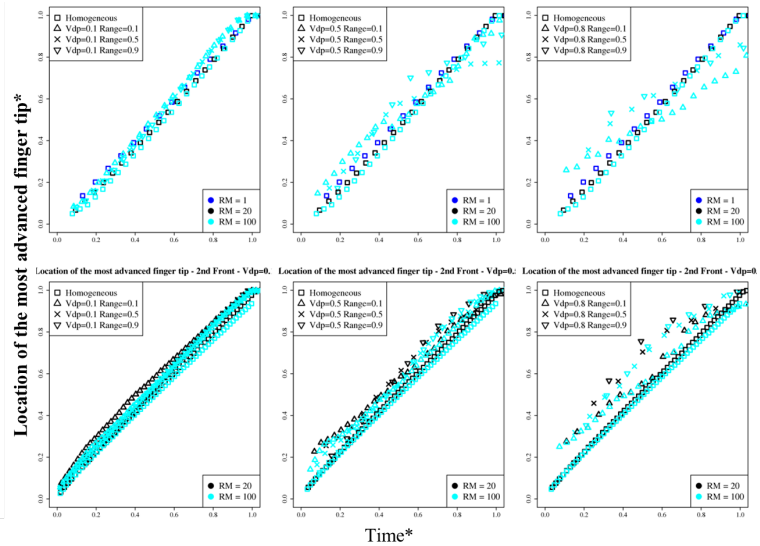

(c) Time evolution of the most advanced fingertip position

Fig. 28: Evolution of the fingering behavior for the downstream (top figures) and upstream (bottom figures) saturation fronts, before water or polymer breakthrough, obtained from 2D polymer flooding simulation with $R_m = 1, 20, 100$ when varying V_{DP} and CL.

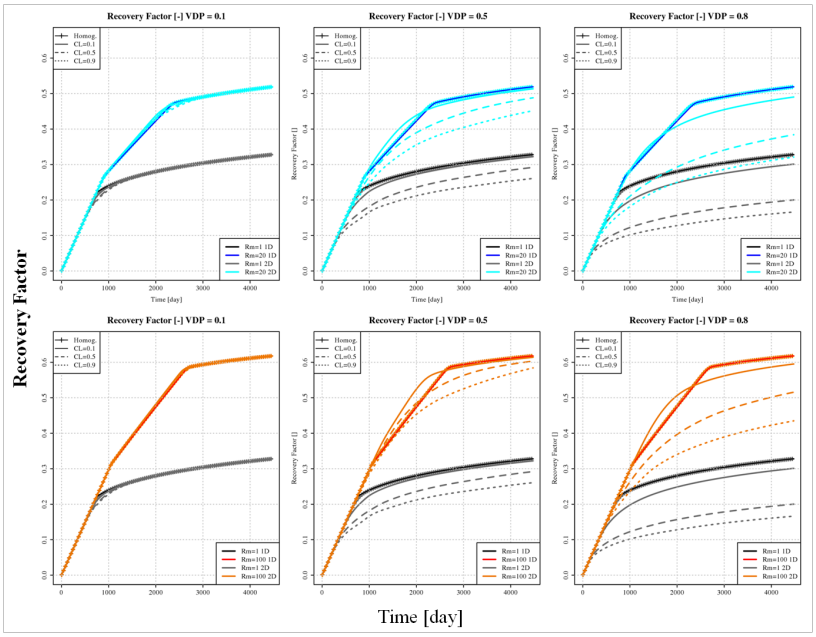

Fig. 29: Comparison of the cumulative oil volume (fraction of the initial oil in place) produced by waterflooding or polymer flooding for $R_m = 100$ as a function of time, obtained from 1D and 2D simulations, when varying the CL and V_{DP} (1D simulations address a homogeneous porous medium).

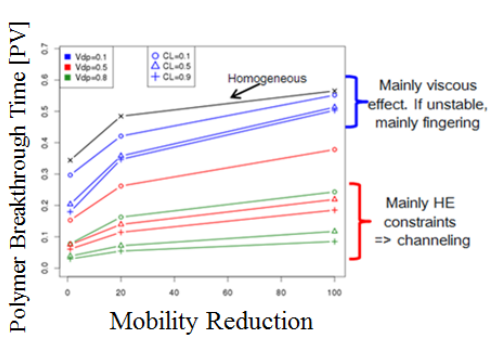

(a) Polymer breakthrough time as a function of mobility reduction.

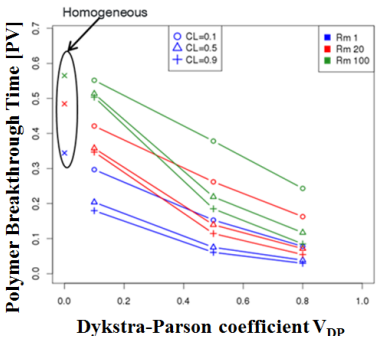

(b) Polymer breakthrough time as a function of V_{DP}.

Fig. 30: Comparison of polymer breakthrough time (expressed in injected pore volume) as a function of mobility reduction and permeability heterogeneity drivers (V_{DP} and CL).

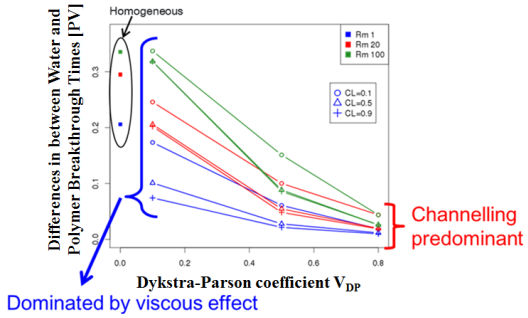

Fig. 31: Comparison of polymer and water breakthrough times difference (expressed in injected pore volume) as a function of mobility reduction and permeability heterogeneity drivers.

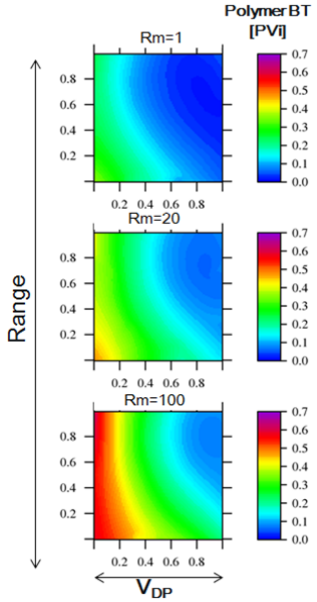

Fig. 32: Polymer breakthrough time as a function of permeability heterogeneity drivers.

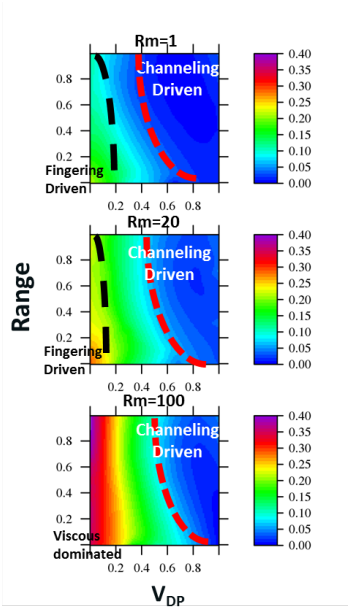

Fig. 33: Polymer and water breakthrough times difference as a function of permeability heterogeneity drivers.